Advanced Steel Construction – Vol. 20 No. 1 (2024) 21–29
DOI:10.18057/IJASC.2024.20.1.3

ANALYSIS OF THE DYNAMIC MECHANISM OF SQUARE TUBULAR T-JOINTS WITH CHORD FLANGES SUBJECTED TO IMPACT LOADING

Peng Deng [1, 2], Dong-Song Chang [2], Xiu-Long Chen [3], Zhong-Yi Zhu [4, *] and Raheel Asghar [2]

[1] *Shandong Provincial Key Laboratory of Civil Engineering Disaster Prevention and Mitigation, Shandong University of Science and Technology, Qingdao 266590, China*

[2] *College of Civil Engineering and Architecture, Shandong University of Science and Technology, Qingdao 266590, China*

[3] *School of Civil Engineering, Southeast University, Nanjing, China*

[4] *Beijing Institute of Architectural Design, Beijing 100055, China*

** (Corresponding author: E-mail: Zhuzhongyi0719@163.com)*

ABSTRACT

This study examines the dynamic mechanical properties of square tubular T-joints with impact loads acting on the chord surface in the joint area. The study first verified the failure modes and behaviors of the specimens under a brace axial force and impact, respectively, where the simulation results demonstrated good agreement with the experimental results. A total of 138 square hollow section tubular T-joint finite element models were divided into T1, T2, and T3 groups based on different tube diameter ratios. The failure modes, displacement-time history curves, and impact force-time history curves were obtained. The results revealed that the joint deformation modes were primarily characterized by significant local indentation at the impact site and junction of the chord and brace, as well as a certain degree of deformation at both ends of the chord. Within a certain range, the preloaded axial force could mitigate the development of plastic deformation, whereas an increased ratio of the drop hammer length to chord diameter exacerbated it. Finally, theoretical analysis was simplified by defining the plastic element set, and the energy dissipation coefficient ψ was proposed to evaluate the impact resistance of square tubular T-joints by analyzing the specific energy changes in the intersecting region (E_I) and at the ends of the chord (E_e).

ARTICLE HISTORY

Received: 29 April 2023
Revised: 31 May 2023
Accepted: 27 August 2023

KEYWORDS

Square tubular T-joint;
Impact loading;
Preloading axial force;
Energy dissipation

1. Introduction

Square hollow sections (SHS) [1–3] are widely used in architecture, bridges, and other long-span structures because of their excellent performance in bending and torsion. The key to connecting all parts of the steel tube component as a whole is the joint, which plays a critical role in the transmission load of the structure. However, owing to the significant disparity between the transverse stiffness of the chord and axial stiffness of the brace, the chord surface near the brace/chord intersection tends to fail [4], leading to local or overall damage to the structure. Tube members may be subjected to various impact loads during their service life (e.g., earthquakes, explosions, or collisions resulting from dropped objects). Currently, studies of scenarios in which the load acts directly on the end of the brace represent simplified analytical models that do not fully correspond to actual structural loading conditions. Consequently, research on the joint response to the load acting on the tubular surface is essential in evaluating the overall response of tubular structures.

Numerical analytical models are crucial in studying the impact performance of tube joints, and reasonable selection of the constitutive model significantly influences the calculation accuracy. Experiments have demonstrated that the mechanical properties of steel, such as the yield stress, ultimate strength, and elongation of the material, differ significantly under dynamic loading from those under static loading, and these properties change under different deformation rates, particularly the strain rate effect [5]. With an increase in the strain rate, the lower and upper limits of the yield strength increase, but the fracture strength decreases [6]. Different material constitutive relationships have been developed to describe accurately the mechanical properties of steel under dynamic loads. The Cowper–Symonds [7] model, which is based on the ideal rigid-plastic model, reflects the relationship between the ratio of the dynamic to the static yield stress, and this model is widely used to predict the strength growth of metals. The Johnson–Cook [8] constitutive model, which is suitable for large strains and high strain rates, reflects the strain-hardening effect of materials and describes their stress flow. A comparison of these models reveals that the Cowper–Symonds model considers the effect of the strain rate on the mechanical properties of steel by introducing the strain rate factor; thus, the model involves fewer parameters and has better applications for topical research.

According to the basic concept of a structure, the structure's mechanical response varies with changes in the load position, and this difference has been studied by researchers. Chen and Shen [9] investigated the dynamic behavior of 226 steel pipes fully clamped at both ends. The results showed that the dented area presented a symmetrical distribution when the load acted on the mid-span, whereas an asymmetrical distribution emerged at one-quarter span and near the supports impact locations. For these types of impact issues, the energy dissipation has been further studied [10], where the failure thresholds were determined to be 655, 395, and 290 J at the mid-span, one-quarter span, and near the supports, respectively. Shen et al. [11] showed that the circumferential stress of a pipe near the end support easily caused the pipeline to buckle on the bottom surface, resulting in shear sliding at the impact location, whereas an impact position at the one-quarter span was susceptible to shear damage at the support [9]. Interestingly, by combining the behavior of axial compression, Al-Thairy et al. [13] found that the plastic-hinge location was not significantly affected by the impact position and was always close to the mid-span, particularly under a large axial load. Regarding the dynamic performance of tubular joint members subjected to impacts, owing to the stress formed by the brace pressure on the chord, it is worth further exploring the impact of the load on the surface of the chord.

Compared with the resistance mechanism of circular tubes, the performance of square tubes is more complicated [12–15]. Square tubes are formed by connecting four steel plates, where the deformation in any plate affects the characteristics of the two adjacent plates [2]. Gupta et al. [16] divided the four steel plates constituting a square tube into horizontal and vertical arms and found that when a static load acted uniformly in the transverse in-plane direction, the middle height of the two vertical arms initially formed hinges, after which second-stage hinges were formed at the four corners. Bin et al. [17] performed hemispherical indenter impact analyses at the mid-span and one-quarter span positions of a rectangular hollow section (RHS) tube with both ends fully clamped. The results indicated that plastic hinges were mainly formed at the indenter impact position and the support, and accompanied by an asymmetric deformation mode when the impact was along the width direction of the upper flange. Furthermore, Bin et al. [18] revealed that the peak force value of the upper flange of the RHS was always constant, even at different impact positions, as the local indentation of the tube could be attributed to the deformation and failure characteristics of the plate. In other words, similar local plastic deformation occurred at the onset of failure. Additionally, the action of the corner in SHS structures should not be ignored. Zhao et al. [19] found that the average tensile yield strength of the corner coupons was 16.8% higher than that of the flat coupons. Shao et al. [4] also revealed that the enhancement effect was beneficial to the transverse stiffness of the chord, increasing the load-bearing capacity of tubular joints, and the larger the corners of the SHS (within a certain

range), the better the strength of the structure [20]. In addition, a reasonable design of the rounded-corner geometry could also significantly improve the energy absorption capacity [21]. Thus, the mechanical behaviors of the corners and plates result in an SHS that differs from a circular hollow section (CHS).

In this study, commercial ABAQUS software was used to perform independent numerical modeling of the static loading [22] and impact tests [23] of SHS T-joints, and the numerical results were compared with experimental curves to verify the feasibility of the finite element (FE) model. Then, 138 FE models of SHS T-joints were developed, including three static specimens and 135 specimens with impact loads acting on the surface of the chord. The three static specimens were used to obtain the ultimate bearing capacity and thus to determine the value of the axial preloading of the brace. The effects of the brace/chord width ratio (β), pre-axial loading (P_{pre}) of the brace, impact velocity (v), and ratio of the drop hammer length to chord width (λ_h) on the performance of tubular structures were preliminarily analyzed, and revealed the failure modes and energy dissipation mechanisms of the SHS T-joints. Finally, the ratio (ψ) of dissipated energy to total system energy is introduced to evaluate the energy dissipation capacity under the aforementioned parameters.

2. Verification of the FE model

2.1. Model information and material properties

According to the test plan, the accuracies of the FE models were verified using static loading [22] and impact tests [23]. The detailed geometries of the specimens are summarized in Table 1, where b, h, t, and L are the width, height, thickness, and length, respectively; R and r denote the outer and inner corner radii, respectively; and the subscripts "0" and "1" indicate the chord and brace components, respectively. The geometric ratios include the ratio (β) of the brace–chord width (b_1/b_0), the ratio (τ) of the brace–chord thickness (t_1/t_0), and the ratio (2Υ) of the chord width to chord thickness (b_0/t_0). The constitutive relationship of the steel is expressed as an elastic–plastic model, as shown in Fig. 1, and the simplified bilinear isotropic hardening model was used for the static specimens. The C–S constitutive model that considers the strain rate was selected for the impact tests and is expressed in Eq. (1).

$$\sigma_{dy} = \sigma_y[1+(\dot{\varepsilon}/D)^{\frac{1}{n}}] \tag{1}$$

where σ_{dy} is the dynamic strength, σ_y is the static strength, $\dot{\varepsilon}$ is the equivalent strain rate, and the rate-dependent constant D and dimensionless parameter n are 6488 s^{-1} and 3.91 [24], respectively. The specific mechanical properties of the steel specimens for the static and impact tests are listed in Table 2.

Table 1
Geometric parameters of the specimens

Specimens	Brace (mm)						Chord (mm)						Geometric Ratios		
	b_1	h_1	t_1	r_1	R_1	L_1	b_0	h_0	t_0	r_0	R_0	L_0	β	τ	2Υ
T-50×100×4-150×150×6 [22]	50.5	100.6	3.96	7.1	10.5	200.3	150.2	151.4	5.950	9.8	13.0	729.9	0.34	0.67	25.25
T-120×120×4-140×140×4 [22]	121.1	121.3	3.91	6.7	9.6	240.5	140.4	141.2	3.994	5.9	8.6	719.0	0.86	0.98	35.16
T8-100c [23]	100	100	5	-	-	500	180	180	8	20	20	1940	0.56	0.625	22.5
T6-60b [23]	60	60	5	-	-	500	180	180	6	12	12	1940	0.33	0.83	30

Table 2
Material properties of the specimens

Specimens	f_y (MPa)		f_u (MPa)		E_s (GPa)	
	Brace	Chord	Brace	Chord	Brace	Chord
T-50×100×4-150×150×6[22]	951.9	1059.1	1098.4	1145.7	200.5	208.5
T-120×120×4-140×140×4[22]	971.4	1008.0	1137.9	1116.4	209.4	208.9
T8-100c [23]	369.8		543.2		208	
T6-60b [23]	369.3		554.5		210	

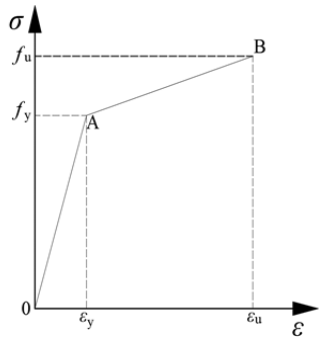

Fig. 1 Bilinear stress–strain curve

2.2. Model simplification

2.2.1. Simplification of static tests

An interface contact between the support and chord was obtained through the Contact pair. The contact properties were determined by defining the normal behavior (hard) and tangential behavior (penalty) with a friction coefficient of 0.3. The reference points (RP-1 and RP-2) were each set at a vertical distance of 20 mm from the bottom of the two supports. The reference points and bottoms of the supports were constrained by coupling, and the degrees of freedom of the two reference points in all directions were limited. The brace and chord were connected by "merge," and the weld simulated welding with a "tie" constraint (the weld design rule was $W_w = t_1$, $W_h = 0.5t_0 + t_1$ [25]). The end of the brace was coupled to the RP-3 point and released the degrees of freedom in the Y direction (i.e., axial direction of the brace). The axial force was loaded by applying the displacement at point RP-3.

2.2.2. Simplification of impact tests

Compared with the static specimens, the impact specimens omitted the end plates on both ends of the chord and coupled the corresponding reference points, where both ends of the chord were completely fixed. The drop hammer was simplified as a rigid body, and the drop hammer and brace end plate contact settings were the same as the support and chord setting properties for the static specimen. With specimens T-120×120×4-140×140×4 and T8-100c used as examples, the simplified models are shown in Fig. 2.

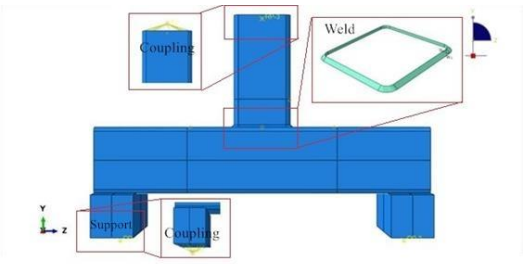

(a) T-120×120×4-140×140×4

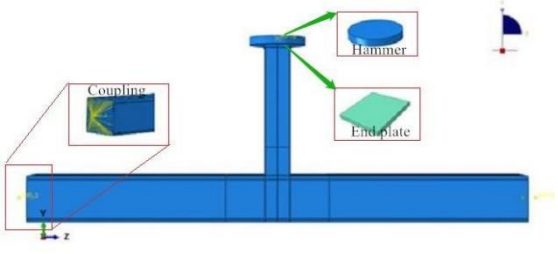

(b) T8-100c

Fig. 2 Simplified specimen models

2.3. Mesh division and sensitivity test

Solid elements are preferred over shell elements for tubular joint members [26–28] because shell elements ignore the stresses along the thickness direction. In this study, all components were modeled using 8-node linear brick solid elements with reduced-integration (C3D8R). The drop hammer and joint meshes were divided using free and structured mesh techniques, respectively. However, because the integrated element (C3D8R) may suffer from hourglass effects in the dynamic analysis, performing local mesh density refinement is necessary. Therefore, based on the sensitivity analysis and accuracy of the FE models, for the joint intersecting area, the study adopted a mesh size of 6 × 6 mm, with the mesh density set to 20 × 20 mm in other areas.

2.4. Verification of FE analytical results

2.4.1. Failure modes

The failure modes of specimens T-50×100×4-150×150×6 and T-120×120×4-140×140×4 are shown in Fig. 3, where the FE results agreed well with the test results. Specimen T-120×120×4-140×140×4 exhibited failure modes of chord face indentation and chord side wall bulging, whereas the difference in β resulted in only chord face failure in specimen T-50×100×4-150×150×6.

Fig. 4 presents a comparison of the experimental and FE models results of specimens T8-100c and T6-60b, where the FE results agreed well with the test results. The failure modes of both specimens were those of chord concavity on upper-face and bulging from web. However, for specimen T6-60b, which had a relatively small width, the indentation depth of the chord upper flange was relatively large, whereas the local buckling deformation of T8-100c was less than that of specimen T6-60b.

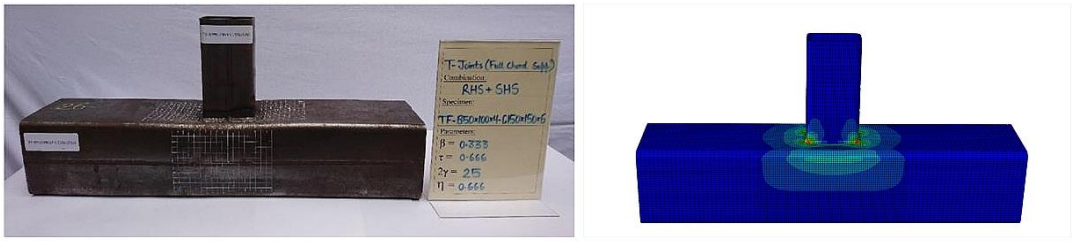

(a) T-50×100×4-150×150×6

(b) T-120×120×4-140×140×4

Fig. 3 Comparison of the FE model and experimental failure modes of static specimens [22]

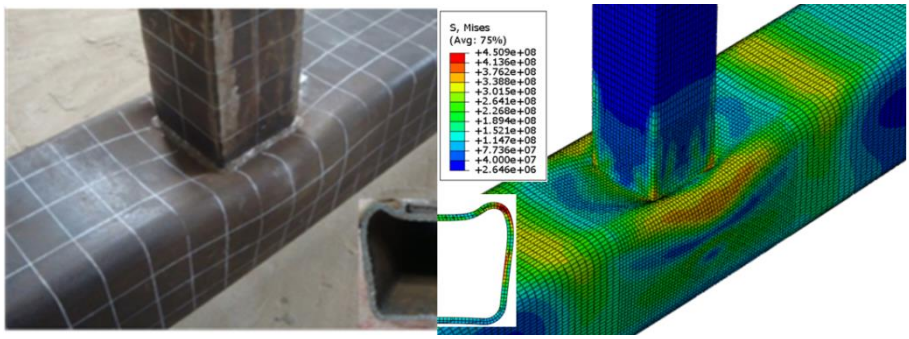

(a) T8-100c

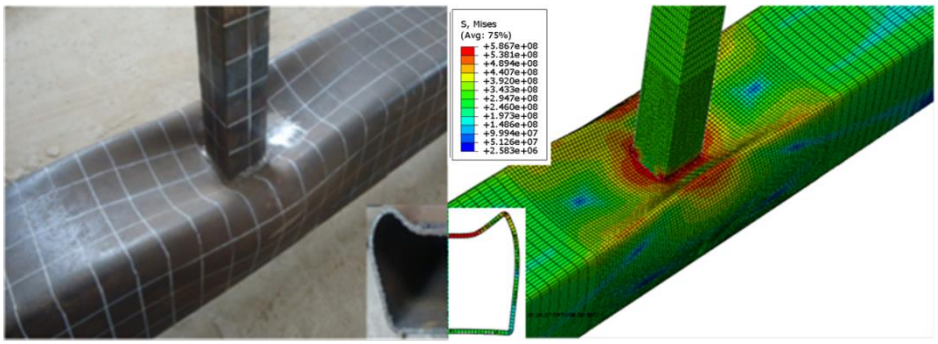

(b) T6-60b

Fig. 4 Comparison of the FE model and experimental failure modes of impact specimens [23]

2.4.2. Verification of the correlation curve

Fig. 5 shows the load versus chord face indentation (relative displacement) curves for the static specimens based on the FE models and test results. The figure shows that specimen T-120×120×4-140×140×4 reached the ultimate bearing capacity, whereas the curve of specimen T-50×100×4-150×150×6 continued to increase. The failure strength of the joint was based on the CIDECT [29] criterion as the first occurrence of P_{ult} (P_u) or $P_{3\%}$. Table 3 presents a comparison of the ultimate bearing capacities derived from the numerical simulation and experimental results. The average error of the values of the FE model was approximately 7% of the experimental values, and the FE results were in reasonable agreement with the experimental results.

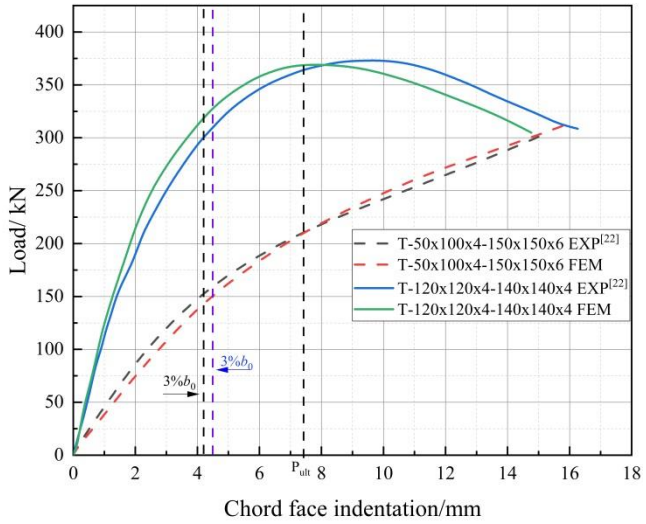

Fig. 5 Comparisons of curves between the FE model and test

Fig. 6 compares the impact force versus time curves for specimens T8-100c and T6-60b. The curve trends show good consistency, and the interval can be divided into four stages, where I–IV correspond to the impact, fluctuation, strengthening, and decline stages, respectively. However, the fluctuation of the FE simulation curves is relatively small in the four stages. Compared with the experimental curves, the impact force values of Stages I and II were higher in the FE simulation. The main reason for this phenomenon is that the FE model ignored the initial stress state of the tube. In particular, specimen T8-100c exhibited greater amplitude fluctuations during the four stages. Still, the shorter impact time was mainly attributed to its increased stiffness and the larger width of the brace/chord as compared with specimen T6-60b.

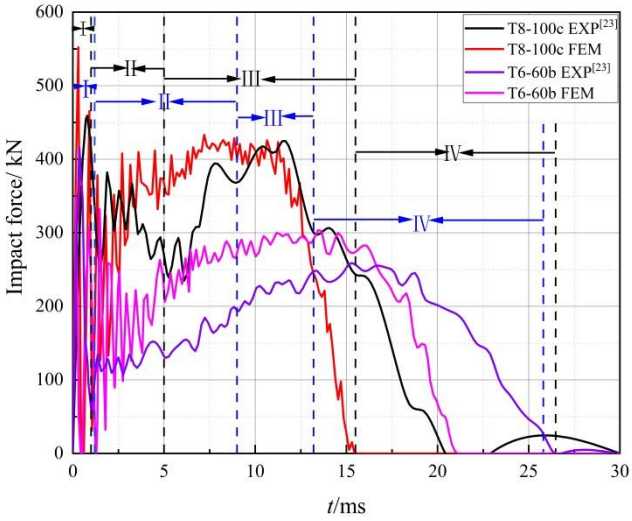

Fig. 6 Time history curves of the impact force under the experimental and numerical models

Table 3
Comparison of the ultimate bearing capacities of the FE models and experimental results

Specimens	P_{max} (kN)	$P_{3\%}$(kN)	$P_{max}/P_{3\%}$	$P_{ult,EXP}$ (kN)	$P_{ult,FEM}$ (kN)	($P_{ult,EXP}$-$P_{ult,FEM}$)/$P_{ult,EXP}$ (%)
T-50×100×4-150×150×6 EXP [22]	-	163.4	-	163.4		-
T-50×100×4-150×150×6 FEM	-	151.2	-	-	151.2	7.4
T-120×120×4-140×140×4 EXP [22]	373.9	346.3	1.08	346.3	-	-
T-120×120×4-140×140×4 FEM	368.38	321.34	1.15	-	321.34	7.2

3. Analysis of FE models of SHS T-joints

3.1. Determination of specimen size

Based on the verified FE model, a T-shaped SHS joint model of a chord subjected to impact was established. The design restrictions complied with specifications outlined in the *Standard for design of steel structures* [25] and *Design of SHS Weld Joints* [30] as well as in practical engineering applications. According to Vander et al. [31], the chord length L_0 should be at least 10 times the chord diameter b_0, as shown in Fig. 7.

A total of 138 FE models were constructed to analyze the effects of the pre-axial pressure (P_{pre}), impact velocity (v), ratio of drop hammer length to chord width ($\lambda_h = l_d/b_0$), and brace–chord width ratio ($\beta = b_1/b_0$) on the impact resistance of SHS T-joints under impact loads. The specific parameters of the specimens are listed in Table 4, including the three static loading specimens and 135 impact specimens. The three static loading specimens (T1-0, T2-0, and T3-0) were used to obtain the static bearing capacities of the specimens and to determine the value of the pre-axial pressure of the brace. The boundary conditions, mesh size, material properties and contact settings between the drop hammer and the joint were kept consistent with the impact specimens [23] in Section 2.

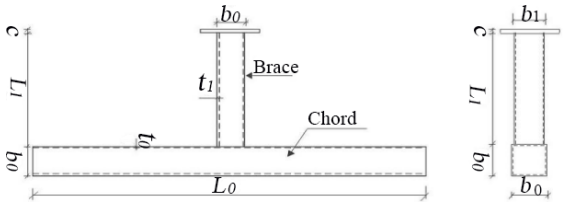

Fig. 7 Geometric properties of the T-joint components

The specimens were named according to the following: T1–T3 denote different β values; 0 P_u, 0.25 P_u, 0.5 P_u, 0.8 P_u, and 1.0 P_u represent the axial pressures of the brace; a, b, and c represent drop hammer impact velocities of 5, 6, and 7 m/s, respectively; and H1, H2, and H3 indicate drop hammer lengths (l_d) of 120, 150, and 240 mm, respectively. For the geometric dimensions of the drop hammer, only the drop hammer length l_d was varied in this study; the other parameters of ω_d, h_d, and r_d were set to 120, 20, and 10 mm, respectively, as shown in Fig. 8.

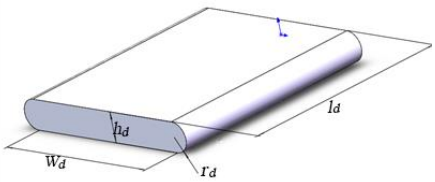

Fig. 8 Geometric properties of the drop hammer

Table 4
Geometric parameters of the FE models

Group	Specimens	Brace (mm)			Chord (mm)			P_{pre} (kN)	v (m/s)	l_d (mm)
		b_1	t_1	L_1	b_0	t_0	L_0			
T1	T1-0	80	5	640	180	6	1940	-	-	-
	T1-0/0.25/0.5/0.8/1.0Pu-a/b/c-H1/H2/H3							0/0.25/0.5/0.8/1.0Pu	5/6/7	120/150/240
T2	T2-0	100	5	640				-	-	-
	T2-0/0.25/0.5/0.8/1.0Pu-a/b/c-H1/H2/H3							0/0.25/0.5/0.8/1.0Pu	5/6/7	120/150/240
T3	T3-0	120	5	640				-	-	-
	T3-0/0.25/0.5/0.8/1.0Pu-a/b/c-H1/H2/H3							0/0.25/0.5/0.8/1.0Pu	5/6/7	120/150/240

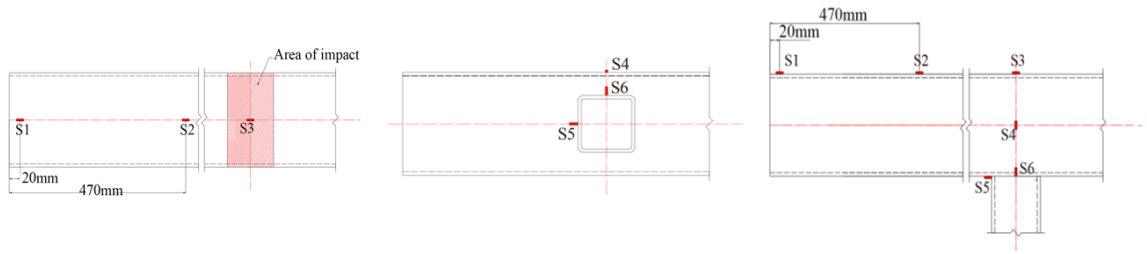

(a) Top view (b) Bottom view (c) Front view

Fig. 9 Arrangement of measuring points

3.2. Load application and position of strain measuring points

The influence of the axial pressure was considered when analyzing the impact resistance of SHS T-joints. Accordingly, two steps are required. In Step One, which employs the static general analysis, the value of the brace preloading axial force is obtained. In Step Two, the dynamic explicit analysis is altered to complete the impact of the drop hammer. The implementation of Step Two depends on the restart technology. The restart function divides the model steps into sets by defining an input file for each set. These sets can be run sequentially, and the information can be transferred from one set to the other, enabling the application of an impact load on the tubular joints after static loading.

Six measurement points were selected to analyze the stress development rule, as shown in Fig. 9. Points S1, S2, and S3 measure the axial stress of the upper flange of the chord, point S4 measures the radial stress at the center of the chord web, and points S5 and S6 measure the axial and radial stresses at the intersecting line of the chord and brace, respectively.

4. Analysis of failure modes

In the studied specimens, failures occurred at the impact area, web, and ends of the chord. A summary of the failure process combined with the research plan enabled two typical working conditions of different preloaded axial forces and ratios of the drop hammer length to chord width to be considered.

4.1. Effects of different pre-axial forces (P_{pre}) on the failure process

The failure histories of the T1-0Pu-a-H1, T1-0.5Pu-a-H1, and T1-1.0Pu-a-H1 specimens are representative to a certain extent and thus can be used for analysis and elaboration. According to the static analysis, when 0.5Pu was applied to the end of the brace, plasticity appeared at the four corners of the intersecting line, and most of the elements at the intersecting area under the action of 1.0Pu exhibited plasticity. Because the specimens did not undergo plastic deformation under 0.25Pu and the plastic state of the 0.8Pu specimens was between that of the 0.5Pu and 1.0Pu specimens, analysis of the aforementioned specimens was omitted. The four moments of the T1-0Pu-a-H1, T1-0.5Pu-a-H1, and T1-1.0Pu-a-H1 equivalent plasticity clouds are shown in Fig. 10 according to the location and order in which plasticity occurred.

When the drop hammer contacted the upper flange of the chord (t = 1.5 ms), T1-0Pu-a-H1 exhibited a more extensive range of plasticity at the impact position, web, and intersection area. The plastic developmental shape of T1-0.5Pu-a-H1 appeared similar, and the plasticity areas were both significantly smaller than those of T1-1.0Pu-a-H1. However, due to chord tension in the T1-0.5Pu-a-H1 specimen, the plasticity scope was somewhat less than that of T1-0Pu-a-H1 and significantly less than that of T1-1.0Pu-a-H1, as shown in Fig. 10(a). Based on the step size calculated by the software, the selected elements began to exhibit plasticity at the chord ends of the three specimens (t = 4.5 ms), as shown in Fig. 10(b). The plasticity area of the T1-1.0Pu-a-H1 specimen almost completely covered the upper flange, bottom flanges and web in the intersecting zone of the joint, whereas the coverage area of the T1-0Pu-a-H1 specimen was slightly smaller, and that of the T1-0.5Pu-a-H1 specimen was smaller still. However, both webs maintained a portion of the elastic scope. As the impact action continued, the bottom flange at both ends of the chord also became plastic (t = 7.5 ms), and the scope of plasticity distribution of the three specimens was similar. Yet the damage to the bottom flange of the T1-1.0Pu-a-H1 specimen was more severe, as shown in Fig. 10(c). Until the drop hammer rebound occurred, as shown in Fig. 10(d) (t = 15 ms), the plastic distribution of the three specimens was nearly identical. However, T1-0.5Pu-a-H1 maintained a slightly elastic scope in the joint area.

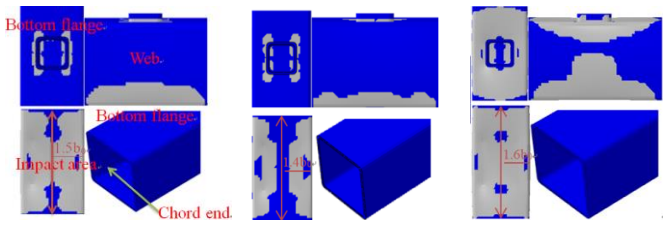

(1) T1-0Pu-a-H1 (2) T1-0.5Pu-a-H1 (3) T1-1.0Pu-a-H1

(a) Moment when the drop hammer contacts the upper flange of the chord (t = 1.5 ms)

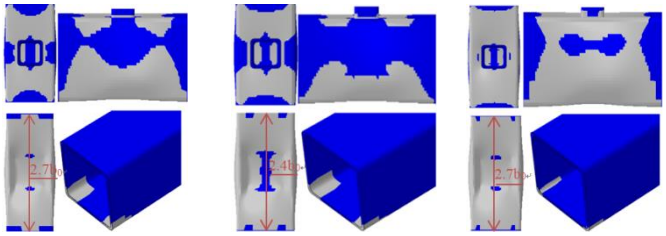

(1) T1-0Pu-a-H1 (2) T1-0.5Pu-a-H1 (3) T1-1.0Pu-a-H1

(b) Moment of buckling of the upper flange at both ends of the chord (t = 4.5 ms)

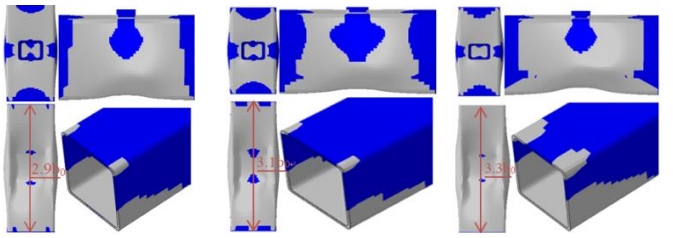

(1) T1-0Pu-a-H1 (2) T1-0.5Pu-a-H1 (3) T1-1.0Pu-a-H1

(c) Moment of buckling of the bottom flange at both ends of the chord (t = 7.5 ms)

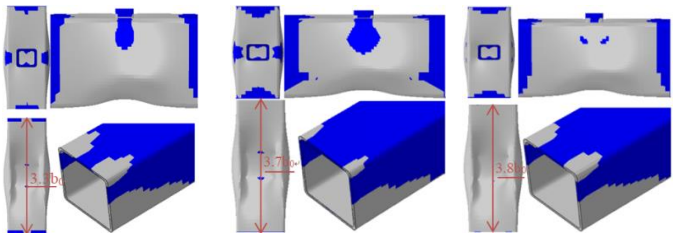

(1) T1-0Pu-a-H1 (2) T1-0.5Pu-a-H1 (3) T1-1.0Pu-a-H1

(d) Moment of drop hammer rebound (t = 15 ms)

Fig. 10 Equivalent plastic development cloud of specimens under different preloads (λ_h = 2/3)

4.2. Influence of the ratio of the drop hammer length to chord width (λ_h) on the failure process

This section examines the cases in which the λ_h values for specimens T1-0Pu-a-H1, T1-0Pu-a-H2, and T1-0Pu-a-H3 were 2/3, 5/6, and 4/3, respectively. Because the failure modes were different from those of the aforementioned specimens, only two states were selected for analysis. When the drop hammer touched the upper flange (t = 1.5 ms), specimens T1-0Pu-a-H2 (λ_h = 5/6) and T1-0Pu-a-H3 (λ_h = 4/3) almost simultaneously exhibited plasticity in the impact area, end of the chord, and web, as shown in Fig. 11(a). By contrast, the plastic scope of T1-0Pu-a-H3 (λ_h = 4/3) at the intersecting area was significantly greater than that of T1-0Pu-a-H2 (λ_h = 5/6) and even more significantly larger than that of specimen T1-0Pu-a-H1 (λ_h = 2/3, as shown in Fig. 10(a)). In particular, the chord end of T1-0Pu-a-H1 (λ_h = 2/3) was entirely in the elastic stage, whereas the other two specimens showed a significant aggravation of damage. Finally, at the moment of hammer rebound, the three specimens exhibited nearly the same degree of failure, as shown in Figs. 10(d) and 11(b). However, a very small area of elasticity was still present in T1-0Pu-a-H1 at the web.

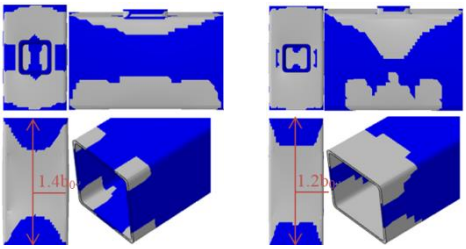

(1) T1-0Pu-a-H2 (λ_h = 5/6) (2) T1-0Pu-a-H3 (λ_h = 4/3)

(a) Moment when the drop hammer contacts the upper flange of the chord (t = 1.5 ms)

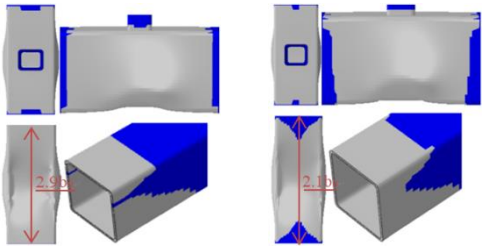

(1) T1-0Pu-a-H2 (λ_h = 5/6) (2) T1-0Pu-a-H3 (λ_h = 4/3)

(b) Moment of drop hammer rebound (t = 15 ms)

Fig. 11 Equivalent plasticity clouds for λ_h of 5/6 and 4/3

5. Time history of the impact force and displacement

5.1. Deformation- time history curves of joints

In this study, the indentation value (Δ) of the upper flange of the chord represents the displacement caused by the impact, which is used to describe the deformation of the joint, as shown in Fig. 12.

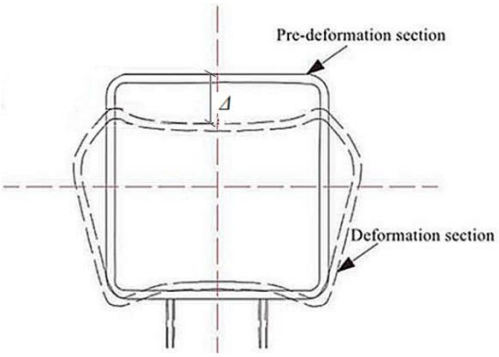

Fig. 12 Calculation of local indentation of the chord upper flange

The displacement-time history curves of the specimens that were subjected to P_{pre} and directly impacted (P_{pre} is 0 Pu) exhibited a similar trend. By contrast, the maximum concave displacement (Δ) of the specimens showed a slight downward trend with increasing P_{pre}, as shown in Fig. 13. Comparing the Δ values in Fig. 13, it can be observed that the effect of P_{pre} on the concave values of the specimens in Fig. 13(b) and Fig. 13(c) is slightly more sensitive than that in Fig. 13(a) but significantly less than the effect of λ_h. The analysis presented in Fig. 11 shows that when λ_h was 5/6 and 4/3, the mechanical characteristics of the joint region were significantly different from those of the specimens with λ_h = 2/3. For instance, the maximum concave displacements of specimens T2-0Pu-a-H1, T2-0Pu-a-H2, and T2-0Pu-a-H3 were 48.2mm, 39.1mm, and 36.1 mm, respectively.

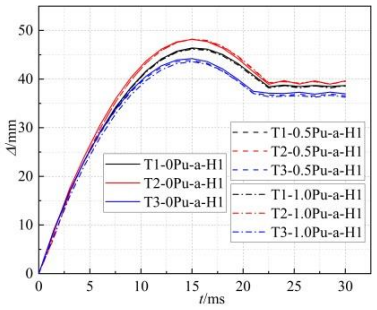

(a) Partial specimen with a drop hammer length of H1

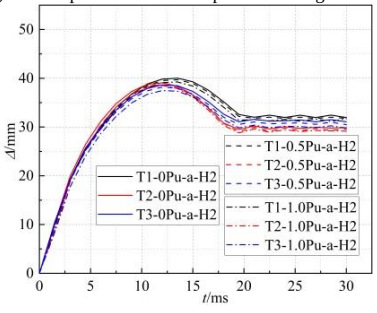

(b) Partial specimen with a drop hammer length of H2

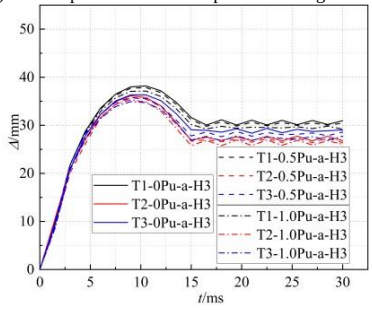

(c) Partial specimen with a drop hammer length of H3

Fig. 13 Displacement-time history curves of specimens

5.2. Impact force-time history curve of joints

As shown in Fig. 10, the equivalent plastic development cloud follows the same basic law. Thus, the impact force-time curves can be divided into four stages:(I) instantaneous impact, (II) impact shock, (III) stable, and (IV) descending, as shown in Fig. 14(a).

As Fig. 14(a) shows, the trends of the curves are significantly different. The overall impact force-time curves of the specimens fluctuate more gently at a drop hammer length of H1, but the total action time is longer. The effect of P_{pre} on the three groups of curves is relatively small, and only in Stage (I) do specimens T1-0.8Pu-a-H2 and T1-0.8Pu-a-H3 exhibit a significant jump. Moreover, the curves are not significantly different in Stages (II)-(IV). Fig. 14(b) shows the effects of variations in λ_h on the impact force-time curves for the same β and P_{pre}. It can be observed that when λ_h = 4/3, the overall value of the impact force-time curve is larger and the impact time is shorter. When v is increased, the overall trend of the curve changes insignificantly, but the action time is significantly increased. Compared with the curves in Fig. 14(c), the curves basically coincide for the specimens at the H1 drop hammer lengths, whereas for the specimens with H2 and H3 drop hammer lengths, the three curves are separated more significantly in Stage (III), and the impact force of the specimens in the T2 group is greater.

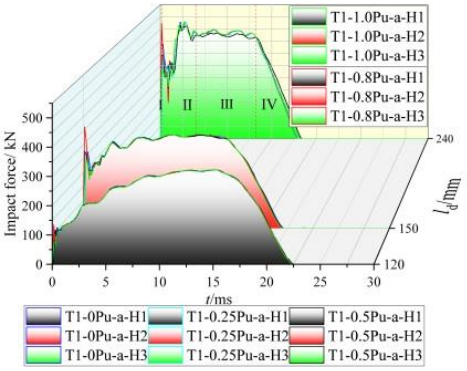

(a) Effect of P_{pre} on the impact force

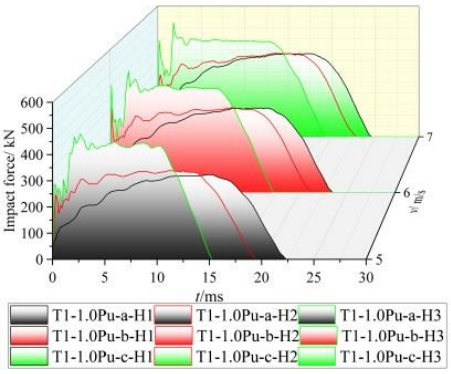

(b) Effect of λ_h on the impact force

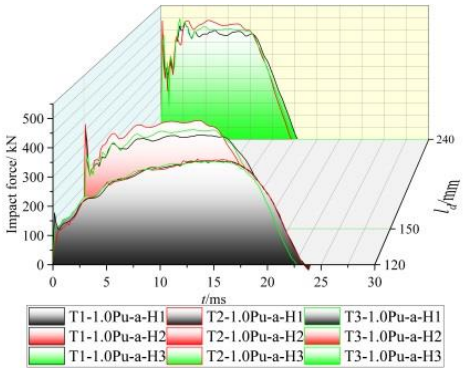

(c) Effect of β on the impact force

Fig. 14 Impact force-time history curves of specimens

6. Evaluation of the impact energy dissipation capacity

6.1. Theoretical analysis of energy dissipation

The impact process actually involves energy transfer and dissipation, and thus analysis of the energy dissipation mechanisms is effective in evaluating the impact resistance performance of tube joints. In the case of an impact on the flange of a T-shaped joint of a square steel tube, the energy conservation equation within the elastic range can be expressed as follows:

$$E_i + E_p = E_c + E_k \tag{2}$$

where E_i represents the kinetic energy of the drop hammer, E_p represents the elastic potential energy of the preloaded brace, E_c represents the elastic potential energy of the deformation of the chord flange, and E_k represents the kinetic energy of the vibrations of the chord and brace.

When the flange of the chord is subjected to an impact load, the chord and brace will undergo elastic deformation, resulting in dissipation of strain energy in the components of the chord and brace. The equation for the strain energy dissipation can be expressed as follows:

$$E_s = \frac{1}{2}\int_V \sigma\dot{\varepsilon}\mathrm{d}V \tag{3}$$

where E_s represents the dissipated strain energy, σ is the stress, $\dot{\varepsilon}$ is the strain rate, and V is the volume of the chord and brace.

The equation for the energy dissipation of the brace preloading under impact loads can be expressed as follows:

$$E_d = 0.5\times(F_p + \Delta F)\Delta\delta \tag{4}$$

where E_d is the energy dissipation, F_p is the preloading force of the brace, ΔF is the increment caused by the impact load on the flange of the chord, and $\Delta\delta$ is the increment of the relative displacement between the brace and chord.

As the failure process proceeds, the plasticity of the chord and brace is developed, as shown in Fig. 10. Energy conservation and dissipation can be expressed as follows:

$$E_i + E_p = E_c + E_k + E_s + E_d \tag{5}$$

After the drop hammer rebounds, the definition can be simplified as follows:

$$E_c + E_k + E_s + E_d = E_l + E_e = E_{diss} \tag{6}$$

where E_l is the energy dissipated by local deformation (concave deformation of the upper and bottom flanges and bulging deformation of the web) and E_e is the energy dissipated by plastic deformation at both ends of the chord.

Significantly, defining the energy dissipation coefficient ψ yields

$$\psi = \frac{E_{diss}}{E_i} \tag{7}$$

Note that because the difference between E_i and E_p is of a large order of magnitude, the effect of E_p is ignored, and the analysis is conducted later.

The coefficient ψ evaluates the storage and loss of energy of an object during the deformation process, which can help us understand the response characteristics of the object under stress, such as its strength, toughness, and durability. This is important for the design and optimization of structures such as square steel tube T-shaped joints.

6.2. Parametric analysis of energy dissipation coefficient ψ

Fig. 15(a) reveals that P_{pre} had no discernible effect on ψ. As P_{pre} increased, the curves of the specimens in groups T1, T2, and T3 remained relatively flat, whereas E_l continued to increase and E_e continued to decrease. However, their changes were comparable, resulting in a nearly horizontal line for ψ. Furthermore, it could be inferred that ψ increased as v increased. Fig. 15(b) illustrates that ψ decreased continuously as λ_h increased with a more pronounced decrease between λ_h = 5/6 and λ_h = 4/3. Simultaneously, E_l

significantly declined, whereas E_e gradually increased. Because the increase in E_e was much smaller than the decrease in E_l ($\Delta E_e < \Delta E_l$), the ψ curve consistently trended downward. Notably, β exerted a more significant effect on ψ than did the other variables, as demonstrated in Fig. 15(c). Specifically, ψ initially decreased and then increased as β increased, with the smallest value appearing at β = 0.56. The energy exhibited a pattern similar to P_{pre} but with greater variability. When β increased from 0.44 to 0.56, the increase in E_l was less than the decrease in E_e ($\Delta E_l < \Delta E_e$), resulting in a downward trend in the curve. However, when β increased from 0.56 to 0.67, the increase in E_l was greater than the decrease in E_e ($\Delta E_l > \Delta E_e$), which produced an upward trend in the curve.

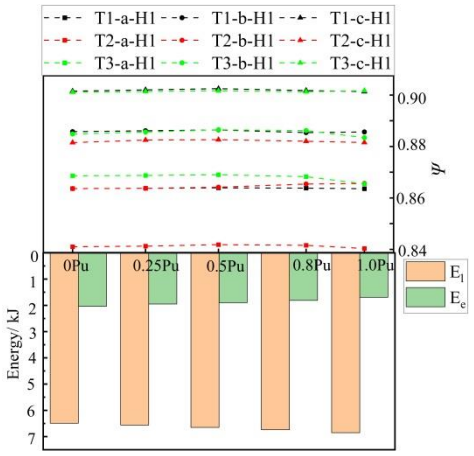

(a) Effect of P_{pre}

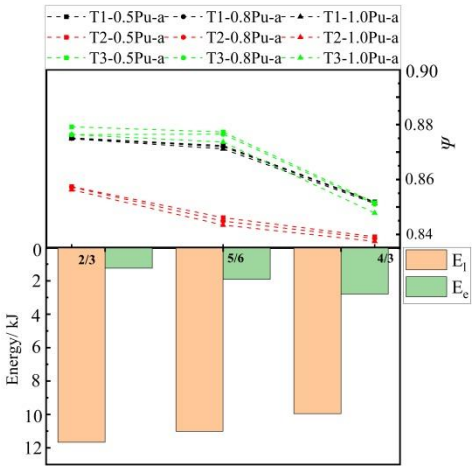

(b) Effect of λ_h

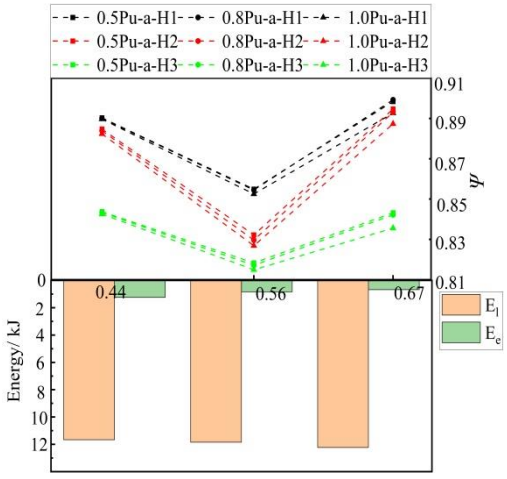

(c) Effect of β

Fig. 15 ψ variation curves of specimens

7. Conclusions

In this study, FE analysis of square tubular T-joints with chord flanges subjected to impact forces was conducted. The failure modes of the tubular joint were studied, and the effects of the pre-axial force, tube diameter ratio, ratio of drop hammer length to chord width, and impact velocity on the mechanical performance of the joint were investigated. The following conclusions were drawn:

1) The damage mode of the joints mainly consisted of local concavity (i.e., local indentation at the impact and intersecting areas) as well as bulging deformation of the web on both sides and plastic deformation at the ends of the chord, in which the effects of λ_h on the displacement values of the local indentation were greatest.

2) The pre-applied axial force of the brace caused tensile stress on the upper flange of the chord. Under the action of the membrane effect, this significantly affected Stage (I) of the impact force–time history curve. When the pre-applied axial pressure did not exceed 0.8 Pu ($P_{pre} \leq 0.8$Pu), the peak value of Stage (I) of the impact force increased with an increase in the pre-applied axial force. However, its effect on the total plastic energy consumption during the impact process was negligible.

3) The impact energy was absorbed through the local concave and plastic deformations at the end of the chord, where E_l played a dominant role. Ψ was used to evaluate the energy dissipation capacity, where ψ continued to decrease with the increase in λ_h. Moreover, the variation of β had a significant influence on ψ; between β = 0.44 and β = 0.56, ψ and β were negatively correlated, while between β = 0.56 and β = 0.67, the curve showed a positive correlation. The values of ψ under different parameters ranged from 0.81 to 0.91, which further confirmed the superior energy absorption capacity of square steel tube joints [32–33].

References

[1] White G.J., Grzebieta R.H. and Murray N.W., “Maximum strength of square thin-walled sections subjected to combined loading of torsion and bending”, International Journal of Impact Engineering, 13(2), 203–214, 1993.
[2] Wardenier J., Packer J.A., Zhao X.L., et al., Hollow Sections in Structural Applications, Bouwen met staal, Rotterdam, The Netherlands, 2002.
[3] Chen Y., Feng R. and Wang J., “Behaviour of bird-beak square hollow section X-joints under in-plane bending”, Thin-Walled Structures, 86, 94–107, 2015.
[4] Shao Y.B., Li T., Seng T.L., et al., “Hysteretic behaviour of square tubular T-joints with chord reinforcement under axial cyclic loading”, Journal of Constructional Steel Research, 67(1), 140–149, 2011.
[5] Zhang R., Zhi X. and Fan F., “Plastic behavior of circular steel tubes subjected to low-velocity transverse impact”, International Journal of Impact Engineering, 114, 1–19, 2018.
[6] Jones N. Structural Impact, Cambridge University Press, 2011.
[7] Cowper G.R. and Symonds P.S., Strain-Hardening and Strain-Rate Effects in the Impact Loading of Cantilever Beams, Brown University, Providence, RI, 1957.
[8] Johnson G.R., “A constitutive model and data for materials subjected to large strains, high strain rates, and high temperatures”, Proceedings of the 7th International Symposium on Ballistics, The Hague, The Netherlands, 541–547, 1983.
[9] Chen K. and Shen W.Q., “Further experimental study on the failure of fully clamped steel pipes”, International Journal of Impact Engineering, 21(3), 177–202, 1998.
[10] Jones N., Birch S.E., Birch R.S., et al., “An experimental study on the lateral impact of fully clamped mild steel pipes”, Proceedings of the Institution of Mechanical Engineers, Part E: Journal of Process Mechanical Engineering, 206(2), 111–127, 1992.
[11] Ng C.S. and Shen W.Q., “Effect of lateral impact loads on failure of pressurized pipelines supported by foundation”, Proceedings of the Institution of Mechanical Engineers, Part E: Journal of Process Mechanical Engineering, 220(4), 193–206, 2006.
[12] Deng P., Chen X., Yang B., et al., “Finite element analysis on the residual bearing capacity of axially preloaded tubular T-joints subjected to impacts”, Structures, 31, 286–304, 2021.
[13] Al-Thairy H. and Wang Y.C., “A numerical study of the behaviour and failure modes of axially compressed steel columns subjected to transverse impact”, International Journal of Impact Engineering, 38(8-9), 732–744, 2011.
[14] Gao F., Xiao Z., Guan X., et al., “Dynamic behavior of CHS-SHS tubular T-joints subjected to low-velocity impact loading”, Engineering Structures, 183, 720–740, 2019.
[15] Bambach M.R., Jama H., Zhao X.L., et al., “Hollow and concrete filled steel hollow sections under transverse impact loads”, Engineering Structures, 30(10), 2859–2870, 2008.
[16] Gupta N.K., Sekhon G.S. and Gupta P.K., “A study of lateral collapse of square and rectangular metallic tubes”, Thin-Walled Structures, 39(9), 745–772, 2001.
[17] Liu B. and Guedes Soares C., “Influence of impact location on the plastic response and failure of rectangular cross section tubes struck transversely by a hemispherical indenter”, Journal of Offshore Mechanics and Arctic Engineering, 139(2), 021603, 2017.
[18] Liu B. and Soares C.G., “Plastic response and failure of rectangular cross-section tubes subjected to transverse quasi-static and low-velocity impact loads”, International Journal of Mechanical Sciences, 90, 213–227, 2015.
[19] Zhao X L and Hancock G J. Square and rectangular hollow sections subject to combined actions[J]. Journal of Structural Engineering, 1992, 118(3): 648–667.
[20] Wang F., “Analysis of punch welding bridge shell fillet based on hyperworks”, Automotive Practical Technology, (07), 31–34, 2012 [In Chinese].
[21] Fu J., Liu Q., Ma Y., et al., “A comparative study on energy absorption of flat sides and corner elements in CFRP square tube under axial compression”, Thin-Walled Structures, 166, 108080, 2021.
[22] Pandey M., Chung K.F. and Young B., “Design of cold-formed high strength steel tubular T-joints under compression loads”, Thin-Walled Structures, 164, 107573, 2021.

[23] Cui P., Liu Y., Chen F., et al., “Dynamic behaviour of square tubular T-joints under impact loadings”, Journal of Constructional Steel Research, 143, 208–222, 2018.
[24] Abramowicz W. and Jones N., “Dynamic axial crushing of square tubes”, International Journal of Impact Engineering, 2(2), 179–208, 1984.
[25] GB50017-2017. Standard for Design of Steel Structures, China Architecture and Buildings Press, Beijing, China, 2017.
[26] Pang H.L.J. and Lee C.W., “Three-dimensional finite element analysis of a tubular T-joint under combined axial and bending loading”, International Journal of Fatigue, 17(5), 313–320, 1995.
[27] Qu H, Huo J, Xu C, et al. Numerical studies on dynamic behavior of tubular T-joint subjected to impact loading[J]. International Journal of Impact Engineering, 2014, 67: 12–26.
[28] Deng P., Zhao S., Zhu Z., et al., “Study on dynamic behavior of tubular T-joints subjected to out-of-plane impact loading”, Journal of Constructional Steel Research, 198, 107556, 2022.
[29] Packer J.A., Wardenier J., Zhao X.L., et al., Design Guide for Rectangular Hollow Section (RHS) Joints under Predominantly Static Loading, Cidect, 2009.
[30] Steel B., Design of SHS Welded Joints, British Steel Welded Tubes, UK, 1991.
[31] Van der Vegte G.J. and Makino Y., “Further research on chord length and boundary conditions of CHS T-and X-joints”, Advanced Steel Construction, 6(3), 879–890, 2010.
[32] Khodaverdlou Z., Basir S.S. and Mohseni P.K., “Numerical and experimental investigation of energy absorption capacity in slotted thin-walled square tube structures”, Journal of the Brazilian Society of Mechanical Sciences and Engineering, 44(8), 368, 2022.
[33] Deng X., Liu F., Cao L., et al., “Energy-absorption characteristics of sandwich corrugated square tubes under axial crushing”, Journal of the Brazilian Society of Mechanical Sciences and Engineering, 44(10), 458, 2022.